AIAA AVIATION Forum
June 27-July 1, 2022, Chicago, IL & Virtual
AIAA AVIATION 2022 Forum

10.2514/6.2022-3984

Low order analysis of panel vibration under ramp-induced shock / boundary layer interaction

Marc A. Eitner[1] and Yoo-Jin Ahn[2] and Mustafa N. Musta[3] and Noel T. Clemens[4] and Jayant Sirohi[5]
The University of Texas at Austin, Dept. of Aerospace Engineering and Engineering Mechanics, Austin, TX, 78712, USA

A thin compliant panel was tested in a Mach 2 wind tunnel. The panel was mounted flush with the tunnel floor and was of dimensions L=121.9 mm (chord), W=63.5 mm (span) and h=0.254 mm (thickness). A 20° compression ramp was placed 5 mm downstream of the model, which induced a shock/boundary layer interaction with fully separated flow over parts of the panel. Full-field deformation was measured using Digital Image Correlation and the surface pressure field was obtained from fast-response pressure-sensitive paint. Analysis of the shock foot motion was performed using a curve-fitting method. Comparison of the shock motion between a rigid and compliant panel case showed no difference in the size of the intermittent region but found that the shock motion over the compliant panel is affected by the panel vibration. Proper Orthogonal Decomposition revealed that the surface pressure is dominated by low-frequency unsteady shock motion, in both cases (rigid and compliant panel). The sixth POD mode clearly shows the streamwise shock foot motion oscillates at the first panel vibration frequency. The surface pressure field upstream of the shock foot is dominated by piston-theory aerodynamics and thus correlated to the slope of the compliant panel. The Sparse Identification of Nonlinear Dynamic Systems algorithm was employed to find low-order representations of the system dynamics. Linear stiffness matrices could be consistently recovered. The measurement noise however prevented extraction of additional relations, such as linear damping matrices or forcing terms from the surface pressure.

I. Nomenclature

L	=	length of panel (in streamwise direction)
W	=	width of panel (in spanwise direction)
h	=	thickness of panel
p_∞	=	freestream static pressure
δ_{99}	=	boundary layer thickness (based on 99% freestream velocity)
σ_a	=	standard deviation of quantity a

II. Introduction

With the development of future flight vehicles such as rockets, missiles or even hypersonic passenger jets come challenges that mostly remain unsolved even in today's age of high-power computing. Multiphysics phenomena such as aerothermoelastic interactions between supersonic flows and compliant structures remain difficult to model. This is primarily due to the large difference of timescales between fluid dynamics, structural dynamics, and heat transfer, which commonly span multiple orders of magnitude.

[1] Postdoc, AIAA member.
[2] Graduate Student, AIAA student member.
[3] Lecturer, AIAA member.
[4] Professor, AIAA fellow.
[5] Professor, AIAA associate fellow.

A common topic of numerical and experimental investigations is the supersonic/hypersonic flow over a compliant panel. Research on this topic has been ongoing for several decades and will continue to be of high relevance in the future [1].

There is an active research community presently working on developing modeling techniques for aerothermoelastic problems, with a strong focus on reduced order modeling. Freydin and Dowell [2] used the Rayleigh-Ritz method to derive a reduced order model of a clamped panel in supersonic flow. They included piston theory aerodynamics and heat transfer to model the dominant physics of the system. They applied their model to a hypersonic test case [3] of a compliant panel inserted in a compression ramp, but neglected SBLI dynamics. Their model was further used to recreate a supersonic test over a compliant panel [4]. The modeling revealed especially the high sensitivity to structural boundary conditions. Brouwer et al. [5] used a nonlinear reduced order thermoelastic model coupled with enriched piston theory aerodynamics. They modeled the response of a buckled panel in supersonic flow and found both experimentally and numerically that cavity pressure and temperature have profound effects on the vibration amplitudes.

The complexity of the aerothermoelastic problem of panel vibration increases dramatically in the presence of shock/boundary layer interactions (SBLI). These can occur from impinging oblique shocks or from detached shocks induced by downstream compression from ramps or fins. Some attempts at modeling of such fluid-structure interactions have been made, see e.g. work by Visbal et al. [6] and Thayer et al. [7], though an accurate three-dimensional coupled model has yet to be created. This is in part because no analytical expressions have been derived that describe the motion of the shock and its coupling with the deformation. Analysis of these systems rely primarily on experimental wind tunnel data. A multitude of recent test campaigns contribute to the understanding of the system dynamics [8] [9] [10] [11] [12] [13] [14] [15] [16].

This paper presents and evaluates a set of experimental measurements that were taken in the spring of 2021 in the supersonic wind tunnel at The University of Texas at Austin. A thin compliant panel was installed into the wall of the tunnel, just upstream of a compression ramp, which induced an SBLI on top of it. Full field techniques such as fast-response pressure sensitive paint (PSP) and stereoscopic digital image correlation (DIC) were used to measure the system behavior. A focus of this paper is to compare rigid panel and compliant panel tests by using low order analysis methods. These comprise of proper orthogonal decomposition (POD) and the sparse identification of nonlinear dynamics algorithm (SINDy). The latter was developed by Brunton et al. [17] and can be used to identify equations of motion from time-histories of dynamic systems.

III. Experimental setup

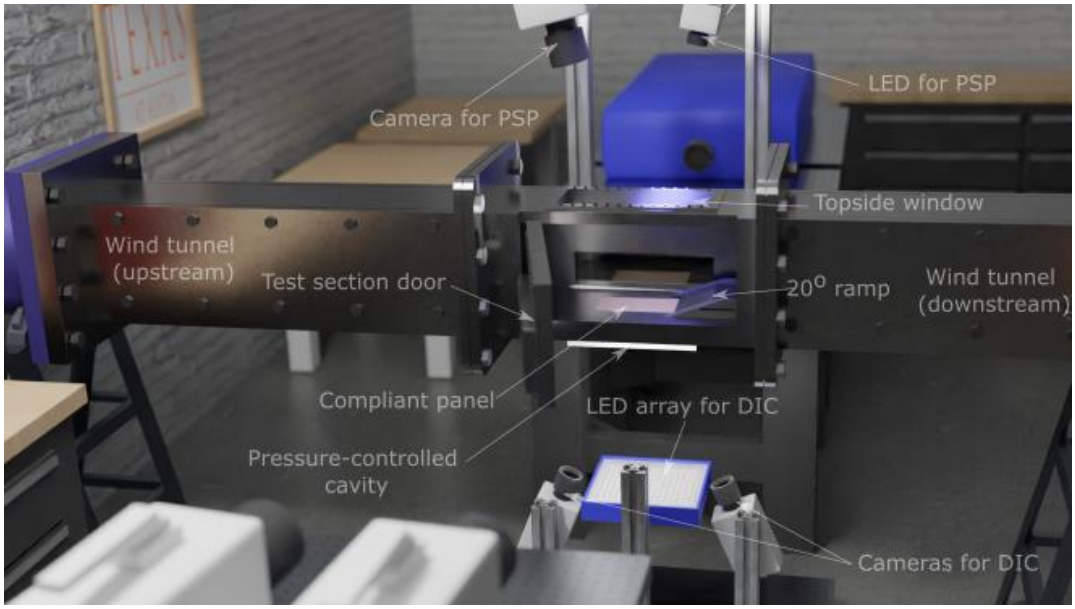

Figure 1: Experimental setup

All tests were performed in the supersonic/hypersonic blowdown wind tunnel at The University of Texas at Austin, depicted in Figure 1. The facility can operate at $M_\infty = 2$ or $M_\infty = 5$, depending on which nozzle block is installed. For this test campaign, all tests occurred at $M_\infty = 2$. The flow was unheated ($T_0 \approx 285 \pm 3\ K$, $p_0 \approx 345 \pm 5\ kPa$) and resulted in test section flow conditions of $U_\infty \approx 514 \pm 3.8\ m/s$ and $\delta_{99} \approx 10.3 \pm 1.4\ mm$. The measured free-stream turbulence intensity was around 1.2%. The test section is rectangular with height and width of 160 mm and 152 mm respectively.

A compliant panel insert was fabricated and inserted into a rectangular cutout in the floor of the tunnel test section, so that it was flush with the floor. The panel was made from 260 brass shim (thickness h=0.254 mm) that was bonded to a brass insert using reflow soldering. The insert was then bolted into the tunnel wall. A metal enclosure was added to the lower side of the tunnel, below the panel, which created a sealed cavity. The lower side of the cavity was outfitted with a window, to allow optical access for two cameras positioned below. The depth of the cavity was 40 mm, which is about 1/3 of the panel length. A 20° compression ramp was placed 5 mm downstream of the panel. The ramp was 25 mm tall, wider than the panel and featured thin fences on the sides, to reduce crossflow effects and prevent interactions with corner vortices. The coordinate system and overview of the panel geometry is shown in Figure 2.

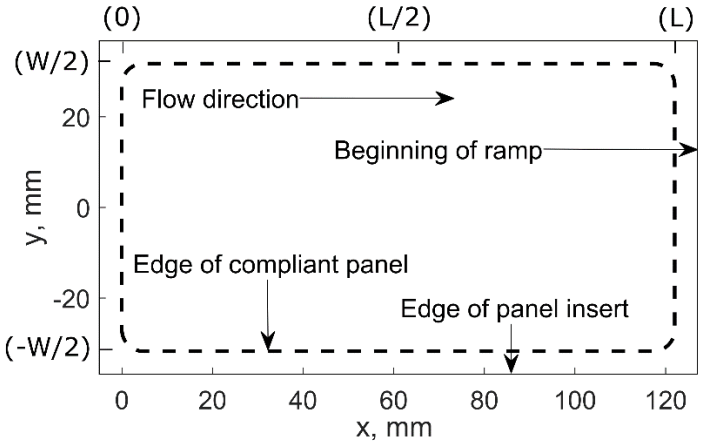

Figure 2: Coordinate system of panel

The deformation of the panel was measured using stereoscopic DIC. A custom-made speckle pattern was designed using the open-source Python code 'speckle_pattern' [18]. It was printed onto white adhesive paper and attached to the lower side of the panel. The two high-speed, monochromatic cameras (Vision Research Miro M310) were equipped with Scheimpflug adapters and 105 mm Nikon lenses. The F-stop value was set to 5.6. Data was recorded at a sampling frequency of $f_s = 5\ kHz$, with 100 μs exposure time and a total duration of 2 s. Image recording, calibration and DIC computation were performed with the software DAVIS 10.2 from LaVision. The noise floor was estimated by recording a still panel and computing its out-of-plane deformation at 100 consecutive time-steps, which resulted in a standard deviation of about 3 μm over most of the panel area.

The flow-facing surface of the panel was painted with a fast-response PSP. The paint was a polymer/ceramic mixture that contained a luminophore, which emits visible light when excited with an LED. This fluorescent effect is quenched in the presence of Oxygen molecules and thus a relation between emitted light intensity and local pressure is created. The paint is mixed on location and multiple layers are sprayed onto the panel using a spray gun. A DC LED lamp mounted above the tunnel shines light (peak wavelength at 460 nm) onto the panel through a window on the top of the test section. The flow-facing side of the panel was imaged using a Photron Nova S, with a 35 mm Nikon lens and an F-stop value of 2. The sampling frequency was $f_s = 20\ kHz$ for test cases with the compliant panels and $f_s = 50\ kHz$ for test cases with a rigid panel and data was recorded for 2 seconds, simultaneously with the DIC. PSP data was later down sampled to $f_s = 5\ kHz$ to facilitate comparison with the deformation data from DIC. This was done by first using a moving average filter (7 time steps centered stencil) and then using every n^{th} data point, where n is either 4 or 10, depending on the original sampling frequency. A common clock signal and trigger ensured that the two data sets (deformation and pressure) were recorded at the same time.

The PSP images were converted to pressure using a calibration curve. A dynamic calibration was obtained from wind tunnel tests on a rigid panel, which featured multiple Kulite pressure transducers along the centerline. The Kulite pressures were then compared to the intensity of the PSP in close vicinity of the Kulites. This was done at multiple locations and resulted in a quadratic calibration curve. An additional static calibration was performed for the PSP, where the pressure in a sealed cavity was reduced and the PSP intensity was compared to a single pressure sensor. Both calibrations resulted in similar curves. The curve static calibration curve was used for the PSP results in this paper.

The cavity pressure p_c (pressure in the cavity below the panel) was controlled using a vacuum pump. Before each test, the cavity pressure was reduced to just over the static pressure in the test section at supersonic conditions. This was done to reduce large static bending deformations during the test, resulting from excessive differences between the mean surface pressures acting on the top and bottom side of the panel. The static pressure in the cavity decreased slightly during the test due to leaks. Over the two seconds of measurement time the cavity pressure varied from $44.8\ kPa$ to $43.1\ kPa$. The freestream static pressure in the test section was calculated from isentropic relations (based on plenum pressure measurements) and was approximately 44 kPa.

IV. Data analysis

A. Rigid panel surface pressure

A baseline for the compliant panel data is established by first analyzing the surface pressure for the test case with a $18\ mm$ thick aluminum panel (referred to as 'rigid panel' in the following discussion) upstream of the compression ramp. The mean surface pressure field is shown in Figure 3-a. The flow over the compression ramp creates a detached oblique shock and induces an SBLI upstream of the ramp. The flow is fully separated and reattaches again on the ramp. This was determined from other experiments, that utilized PSP on the ramp [12] and particle image velocimetry (PIV). The separation point is likely located around $1.5\ \delta_{99}$ upstream of the compression corner, at $x/L \approx 0.9$. The flow is primarily two-dimensional, though there is a slight distortion in the lower half of the pressure field. Unsteadiness in the surface pressure results from two effects: The turbulent fluctuations of the boundary layer as well as the low-frequency unsteady motion of the SBLI [19]. A plot of the standard deviation of the surface pressure is shown in Figure 3-b. A band of large pressure fluctuations is visible at the location of the SBLI. It can be shown that the streamwise extent of this region corresponds to the intermittency region of the shock foot.

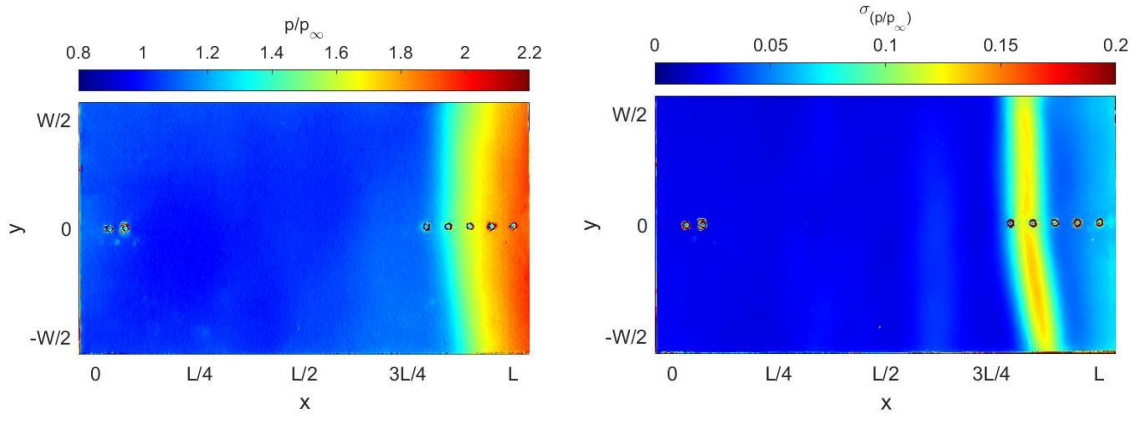

Figure 3: Surface pressure on rigid panel, (left) mean and (right) standard deviation, flow from left to right

A surrogate shock foot can be tracked using the surface pressure data. In this paper, the shock foot motion is tracked in the following way:

1. The pressure (from PSP) is extracted along a streamwise line near the center, but sufficiently far away from the Kulite holes (at $y = W/10$). This pressure line is shown in Figure 4-a along with the standard deviation (rms of the mean-subtracted pressure along that line for all time-steps).
2. The pressure is spatially smoothed using a moving average filter with a stencil length of L/10

3. Two linear regimes are fit to the data, one that fits the mostly constant pressure upstream of the shock foot and another with a positive slope that fits the shock-induced pressure rise (indicated as black lines in Figure 4-a.)
4. The boundary where the two linear regimes intersect is recorded as the surrogate shock foot x_s. The process is repeated for all time steps.

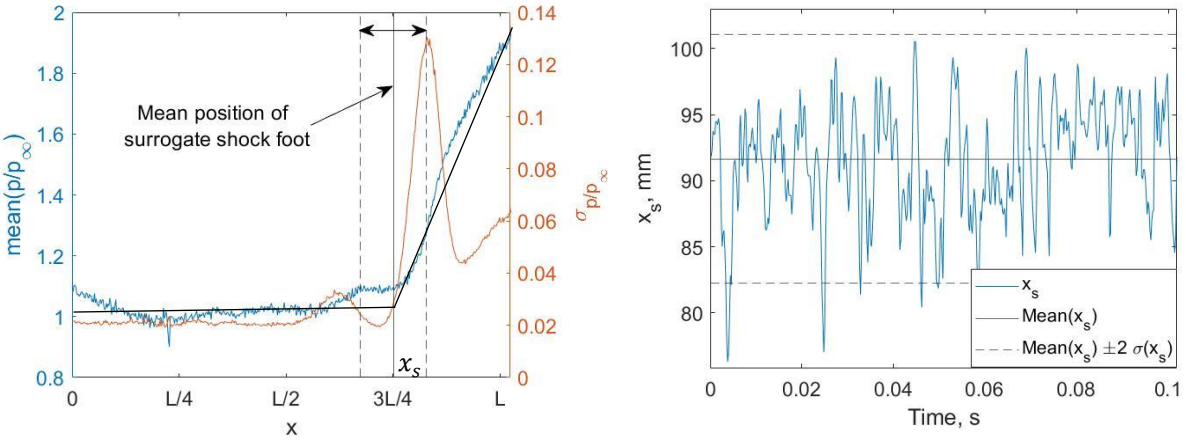

a) b)

Figure 4:Surrogate shock foot motion, (a) comparison to mean and standard deviation of pressure, (b) time history

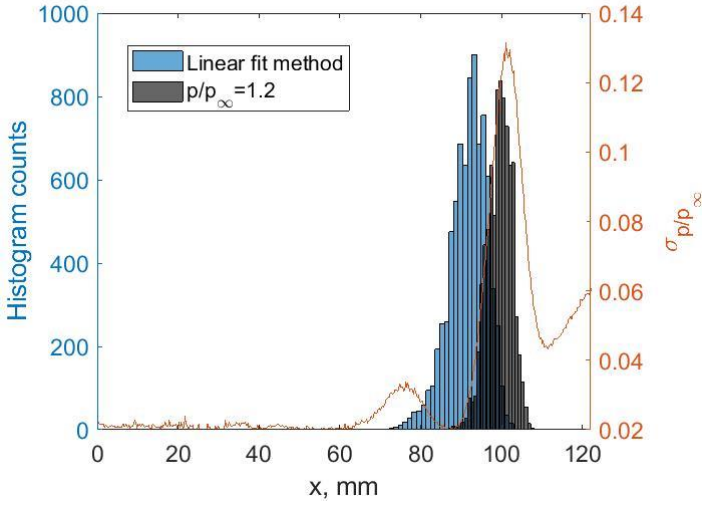

Figure 5: Histogram of shock motion extracted with two different algorithms

The time-history of the surrogate shock foot is plotted in Figure 4-b. The mean location is at $x = 91.7\ mm$ or $x/L = 0.75$. The unsteadiness of the shock foot is characterized through its standard deviation, which is $\sigma_{x_s} = 4.7\ mm$ or $\sigma_{x_s} = 0.04/L$. Note that the values in the plot are in mm, rather than normalized by panel length, to better visualize small motion. Shown in Figure 4-a are the mean and standard deviation of the surface pressure over the

length of the panel at the location $y = W/10$. Note that these are simply a 2-dimensional visualization of the data shown in Figure 3. The mean position of the surrogate shock foot is also plotted along with a range corresponding to ± 2 standard deviations σ_{x_s} of the shock foot motion. Note that the position of the shock foot is somewhat arbitrarily defined, based on the algorithm used. The focus here is however placed on the upstream and downstream motion of the shock foot. It is evident that this intermittent region of the shock foot is of similar width as the dominant peak in the pressure standard deviation. Thus, it seems that the large pressure fluctuations are indeed a result of the unsteady motion of the shock foot. For comparison, the shock foot motion was also extracted using the common method of defining a pressure threshold (p/p_∞=1.2) and tracking its corresponding x-location. This was done for the same y location as the linear fit method described above and the two results are compared. From the time-histories of both shock motions, the histogram was computed and plotted in Figure 5. When using the threshold method, the histogram is narrower, indicating a smaller streamwise motion. The standard deviation is only 3.0 mm. The advantage of the line fitting method is that it utilizes the entire pressure distribution (along a line), and thus is less sensitive to noise in the PSP. The classical method only relies on the pressure at a single location, which might require significant amounts of spatial smoothing to. Based on the high quality of the PSP measurements in this paper, little smoothing was needed to make the classic pressure threshold method work.

The unsteadiness of the SBLI can also be characterized in the frequency domain. Shown in Figure 6 is the power spectrum of the shock foot motion, whose time-history is shown in Figure 4-a. The power spectral density $G(f)$ was multiplied by the frequency and normalized by the variance of the shock foot motion. The motion is dominated by low frequencies below 1 kHz. Note that the shock motion was calculated using the down sampled PSP data, thus the Nyquist frequency is 2.5 kHz. The plot also shows the power spectrum of the surface pressure at the location of highest pressure fluctuations ($x = 3L/4$, $y = W/20$). The surface pressure was averaged spatially over a region of 7x7 pixels, which roughly corresponds to the surface of a Kulite transducer. This computation was done before down sampling the data, thus the original sampling frequency of $f_s = 50\ kHz$ could be used to generate a power spectrum covering a larger frequency band. The power spectral density $G(f)$ of the surface pressure (in psia) was multiplied by the frequency vector and normalized by the local variance of the pressure. Again, the plot shows that most of the energy is contained in a low-frequency band below 1 kHz.

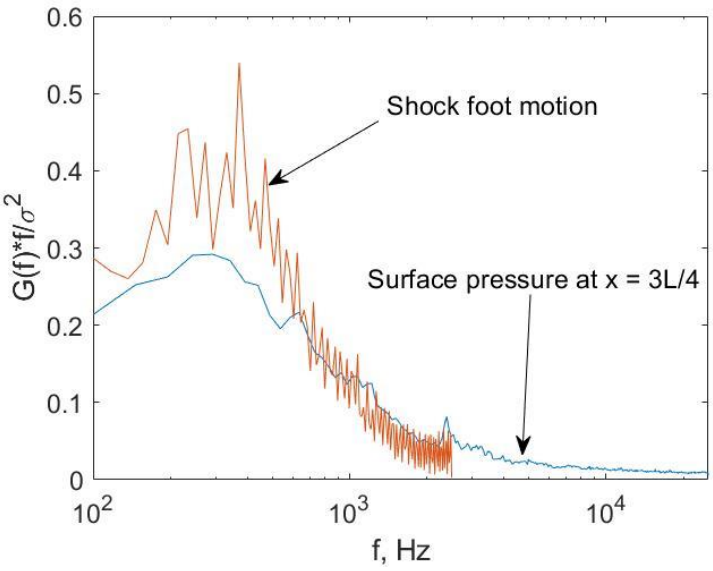

Figure 6: Power spectra of shock foot motion and surface pressure show low-frequency SBLI unsteadiness

B. Low order representation of the rigid panel surface pressure

In this section, an attempt is made at creating a data-driven, low-order representation of the surface pressure dynamics. First, proper orthogonal decomposition is used. Next, a custom single parameter function is created with the goal to capture the dominant shock motion.

The surface pressure data from the rigid panel case is first spatially smoothed using a Gaussian kernel with a standard deviation of 3 px. The pressure around the Kulite sensor holes is excluded (set to 'NaN' in MATLAB). Next, the POD is performed, using the entire length of the data set:

$$[U][S][V] = [P],$$

Where the matrix $[U] \in \mathbb{R}^{N\times N}$ contains the mode shapes, $[S] \in \mathbb{R}^{N\times M}$ contains the singular values along its diagonal, $[V] \in \mathbb{R}^{M\times M}$ contains the time coefficients / time-histories and $[P] \in \mathbb{R}^{M\times N}$ contains the time histories of the measured surface pressure. N are the number of time-steps and M represents the spatial degrees of freedom.

The first three POD modes are shown in Figure 7 a-c. The first mode has a peak near the area of largest pressure fluctuations and resembles the plot of the pressure standard deviation in Figure 3-b. It is mostly symmetric about the centerline, though the slight asymmetry follows that of the pressure fields plotted in Figure 3. The second POD mode is mostly antisymmetric, with a slight offset towards positive y-values, opposing the offset of the first POD mode towards negative y-values. The third POD mode is again mostly symmetric and highlights the pressure fluctuations in the separated flow region (downstream of the shock). The first 100 singular values are plotted in Figure 7-d and are normalized by the sum of all singular values. The first three modes combined contain only 13% of the overall energy in the system and the first mode by itself is only responsible for 4.8%. The time-history of the first mode is dominated by low-frequency motion very similar to that shown in Figure 6 (plot omitted for brevity).

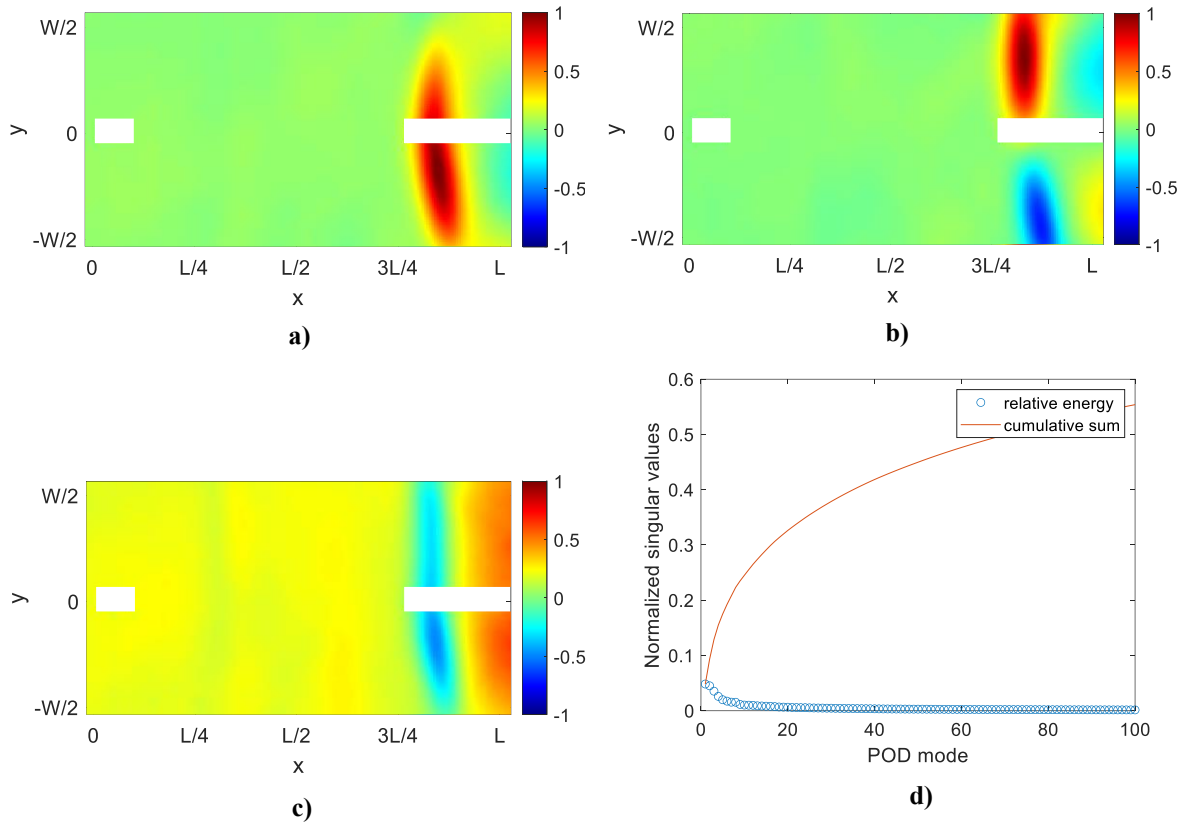

Figure 7: POD of rigid panel surface pressure; (a) first mode, (b) second mode, (c) third mode and (d) singular values

The problem with the POD representation is that the streamwise motion of the shock foot cannot be adequately represented with spatially constant modes. For this reason, a different low-order representation is proposed, that is based on a one-dimensional ramp function, which changes its location based on the tracked shock motion. This model assumes that the pressure upstream of the shock is undisturbed and equal to the freestream pressure and the pressure rises linearly downstream of the shock. In mathematical form, the surface pressure along the x-direction is given as:

$$\frac{p(x,t)}{p_\infty} = 1 + \alpha R(x - x_s(t))$$

The function $R(x - x_s)$ is the ramp function, which is zero for values of $x < x_s$ and has a slope of unity for values $x \geq x_s$. The factor α modifies the slope and the shock location x_s defines the beginning of the pressure increase. If the slope parameter α is fixed, the only variable is x_s. This function therefore accounts for the streamwise motion of the shock foot, which is responsible for most of the pressure fluctuations in the system. The question remains of how to determine the value α. Shown in Figure 8-a are ensemble averaged pressure distributions taken at $y = W/10$. The ensemble averages are computed by determining the 100 largest and lowest values of the previously extracted shock position x_s and then averaging the pressure distributions at the corresponding time steps. Based on the mean pressure curve the rise in pressure downstream of the shock foot can be modeled approximately as linear. However, the slope changes drastically when the shock is at the upstream or downstream position. This means that the slope needs to be a variable that changes with time, thus creating a 2DOF model, which is not desired. However, it can be shown that the slope parameter α has a direct relation with the shock foot position x_s. These two quantities are plotted against each other in Figure 8-b. A quadratic curve can be fit to this cluster plot, to obtain the relation between α and x_s:

$$\alpha(x_s) = 0.1561 - 0.003979x_s + 2.851 \cdot 10^{-5}x_s^2$$

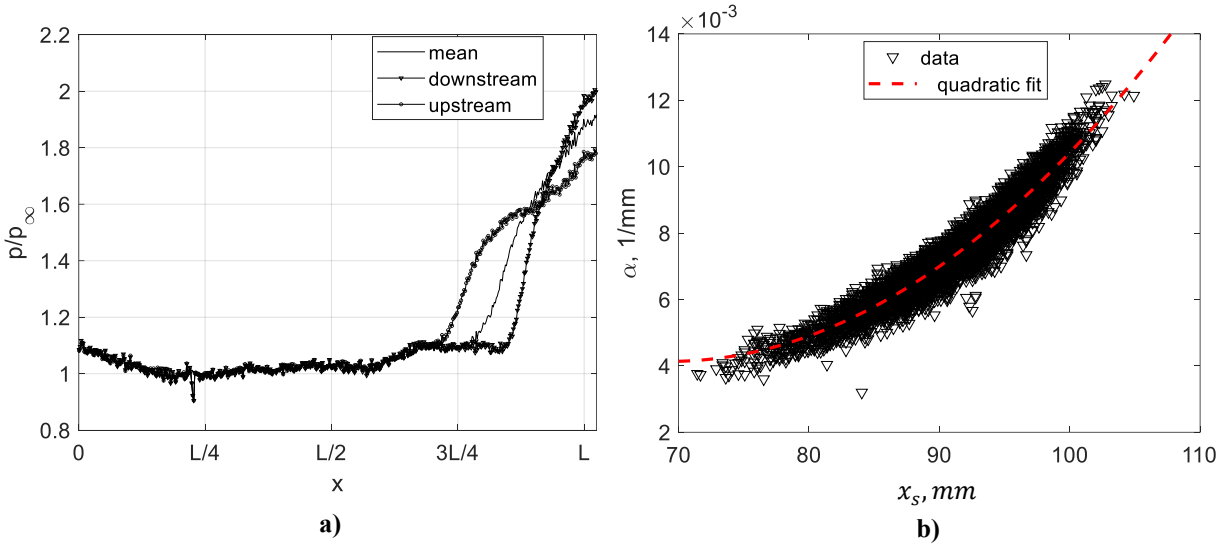

Figure 8: Relation between shock position and pressure increase; (a) ensemble averaged pressure at y=W/10, (b) relation between linear slope α and shock position

The resulting pressure function is then simply expanded along the y-direction to result in a full-field pressure map for each time step (the pressure only varies in the streamwise direction). This model is presented here as a very simplistic alternative to the POD decomposition. It was developed to serve as the dominant pressure time-history for use in the SINDy algorithm. It turned out that none of the low order representations of the pressure field (including POD modes) were able to yield consistent results, though it is possible that measurement noise remains the primary reason for that. Thus, this model is left here for future reference, but not further discussed throughout this paper.

C. Compliant panel test results

1. Structural deformation

The thin brass panel experiences both static and dynamic forcing as a result of the surface pressure acting on it. The mean pressure on the flow-facing side is higher than the cavity pressure and thus the panel deforms statically into the cavity. The quantity that is computed from the DIC technique is the out-of-plane bending deformation. The mean value is shown in Figure 9-a and is normalized by the panel thickness h. The panel deformation reaches its lowest point (w/h =1.6) near the downstream end of the panel, since that is where the high pressure region downstream of the shock resides. To visualize the vibration, the standard deviation of the panel motion is calculated at each spatial point and plotted in Figure 9-b. Most of the vibration energy is contained in the first mode and the standard deviation of the motion reaches 82% of the panel thickness near the center.

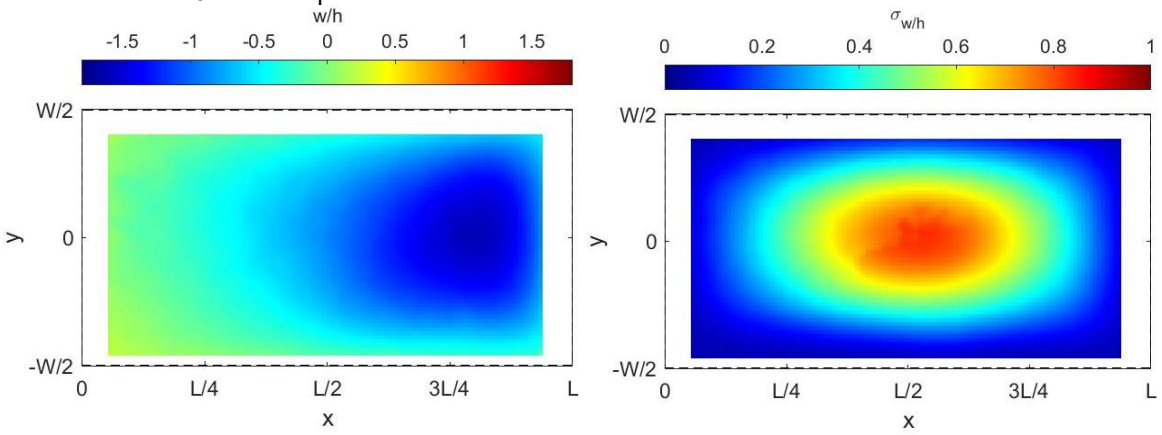

Figure 9: Out-of-plane bending deformation measured using DIC, (a) mean and (b) standard deviation

The natural frequencies of the first five bending modes of the compliant panel under flow conditions with the ramp are listed in Table 1 for completeness. They were obtained from the measured data using an operational modal analysis algorithm known as Complexity Pursuit [20]. The naming of the modes is based on the amount of half waves in the x and y direction, e.g., mode 2-1 has two half sine waves in the streamwise (x) direction and one half sine wave in the crossflow (y) direction.

Table 1: Natural frequencies of compliant panel in flow conditions

Mode	1-1	2-1	3-1	4-1	1-2
Frequency, Hz	494	708	967	1245	962

2. General comments on the compliant panel surface pressure

The surface pressure of the compliant panel test case is analyzed in this section. The mean static pressure field is plotted in Figure 10-a. Upstream of the shock foot, the pressure is slightly below the nominal freestream pressure due to the panel curving downwards and away from the flow (into the cavity). This is a result of the cavity pressure being lower than the mean surface pressure field during the tunnel run. This leads to a flow expansion which induces a pressure reduction. On the outer edges of the panel, the surface pressure is approximately equal to the freestream pressure since the edges are rigid and thus undeformed.

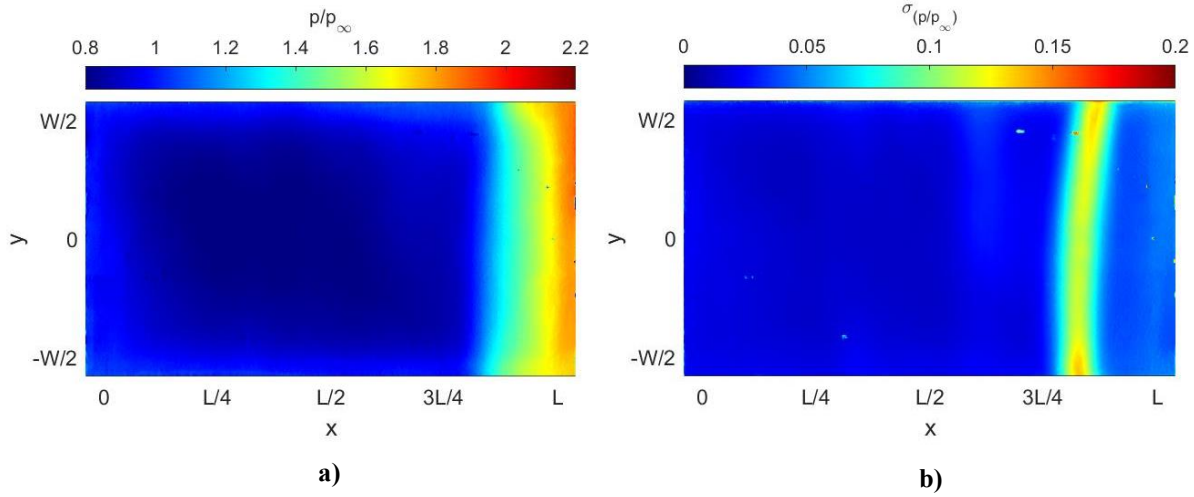

Figure 10: Compliant panel surface pressure; (a) mean and (b) standard deviation

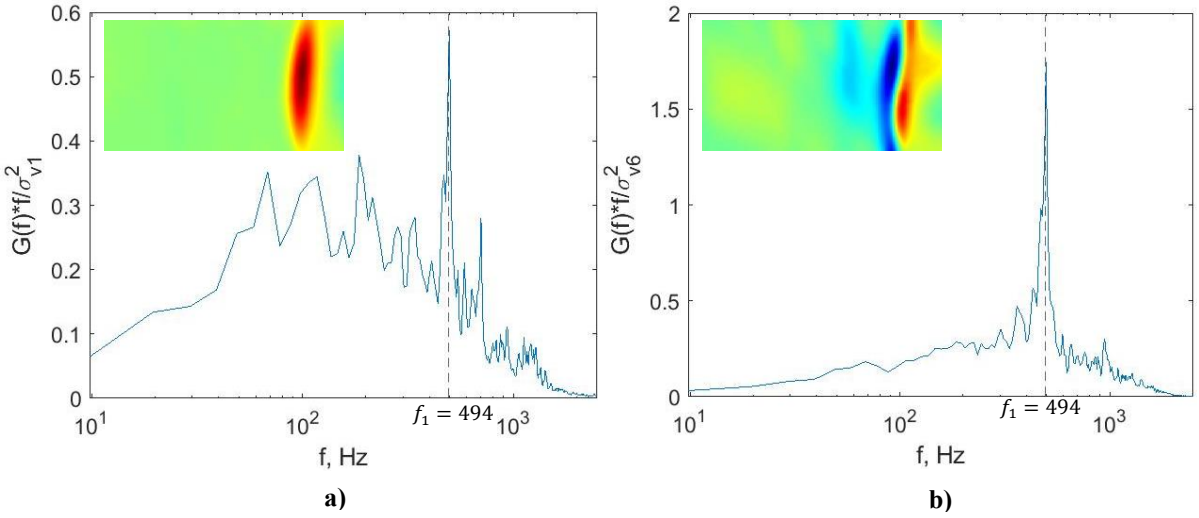

Figure 11: Power spectra of (a) first and (b) sixth surface pressure POD modes

The surface plot of the pressure standard deviation $\sigma(p/p\_\infty)$ is provided in Figure 10-b. The slight asymmetry that was observed in the rigid panel case is now reversed – the top part of the pressure field seems skewed in the downstream direction. Since the ramp was moved and installed several times in-between the rigid and compliant panel test cases it is possible that very slight misalignment of the ramp might be the cause of these asymmetries and differences between the rigid and compliant test cases. The peak pressure fluctuations occur near the edges (near $y = \pm W/2$), which indicates that the compliance of the panel might play a role in the reduction of the pressure fluctuations.

The POD modes of the surface pressure on the compliant panel were computed and compared to the rigid panel case. The low order modes resemble mostly those of the rigid panel and their relative energy is comparable as well. The mode shapes are listed in the appendix for completeness. There is strong evidence that the panel vibration influences the surface pressure. This can be seen in the power spectrum of some POD modes. Figure 11-a shows the power spectrum of the first POD mode, along with an image of the mode shape, which resembles closely that of the rigid panel case, as mentioned previously. The power spectrum is dominated by a band of low frequency unsteadiness, with a single significant peak at the first vibration frequency. While this peak is noticeable, it cannot be said that it fully dominates the surface pressure fluctuations. On the other hand, the power spectrum of the sixth POD mode is plotted in Figure 11-b. This mode oscillates solely at the first panel vibration frequency and the mode shape indicates a streamwise motion.

3. Shock foot motion over compliant panel

Since it was previously concluded that the low-frequency shock foot unsteadiness is the primary reason for the region of large pressure fluctuations, the shock foot is analyzed next. As before, the shock motion is extracted along a single line at $y = W/10$. The shock foot tracking procedure described above is again used for the compliant case. The mean shock position is calculated as 93.6 mm or $x/L = 0.77$, which is about 2 mm downstream of the rigid panel case. The standard deviation of the shock foot motion is $\sigma_{x_s} = 4.7\ mm$, which is the same as in the rigid panel case.

While the compliance shows no effect on the extent of the shock foot motion, there is a clear change visible in the frequency domain. Figure 12 shows the power spectrum of the shock foot motion for the compliant panel case. The general trend that was observed in the rigid panel case is conserved, meaning the system is still dominated by low-frequency unsteadiness. In addition, there are multiple peaks visible, which coincide with the resonant frequencies of the compliant panel. The first three panel bending mode shapes and their frequencies are added in Figure 12. Thus, the panel vibration seems to affect the motion of the shock foot. This effect has been experimentally shown in previous publications [8] and is consistent across multiple panel thicknesses, panel materials and shock tracking algorithms. It has not been shown that the oblique shock also exhibits these clear oscillatory frequencies though the shock foot and oblique shock are closely related. Further flow field imaging (Schlieren or particle image velocimetry) is needed to show such a relation.

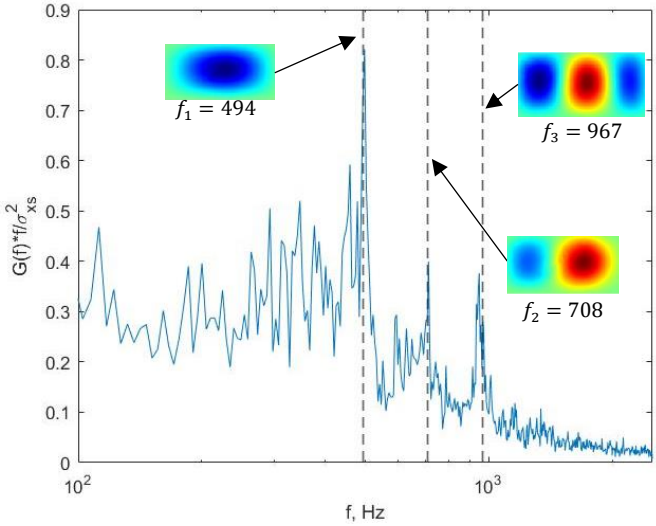

Figure 12: Power spectrum of shock foot motion shows peaks near panel vibration modes

4. Upstream pressure-deformation relations

The previous section discussed the relation between the shock foot and the panel deformation. The region upstream of the shock foot is dominated by a superposition of two effects. Broadband pressure fluctuations that are present in the turbulent boundary layer create spatially and temporally uncorrelated surface pressure dynamics. Due to the deformation of the panel, the attached flow is slightly compressed or expanded based on the local slope $\partial w/\partial x$. This results in spatially and temporally correlated surface pressure fluctuations at tonal (single) frequencies. The relation between panel slope (in streamwise direction) and induced surface pressure variation can be explained by first-order piston theory [20]. In a previous publication by Eitner et al. [8], the theoretical predictions showed reasonable agreement between the pressure fields and those predicted by first-order piston theory. Here, a different approach is taken, that uses a modal projection technique to demonstrate the slope-pressure relation. Figure 13(a-b) show the first two amplitude-normalized bending mode shapes of the compliant panel. The streamwise slope of these mode shapes is computed and depicted below them in Figure 13(c-d). The plots also show a dashed rectangle, which marks a region $\Omega_{u/s}$ upstream of the mean shock position ($x < 3L/4$). The pressure field that overlaps with this region is then projected onto the slope region $\Omega_{u/s}$ which results in a modal coordinate for the pressure:

$$q_i(t) = \left\{\frac{\partial \Phi_i}{\partial x}\right\}^T_{\Omega_{u/s}} \cdot \{p(t)\}_{\Omega_{u/s}}$$

This is simply a dot product between two vectors that cover the same area $\Omega_{u/s}$, the first contains the slope of the mode shape Φ_i and the second vector is the surface pressure field at time t. The power spectral density $G(f)$ of each modal coordinate q_i is shown in Figure 13(e-f). The spectra clearly show a dominant peak that coincides with the resonant frequency of the corresponding mode. Note that in each plot, a vertical dashed line is overlayed, which denotes the respective resonant frequency. This good agreement demonstrates that the surface pressure field upstream of the shock foot does indeed correlate with the slope of the panel, which agrees with first-order piston theory.

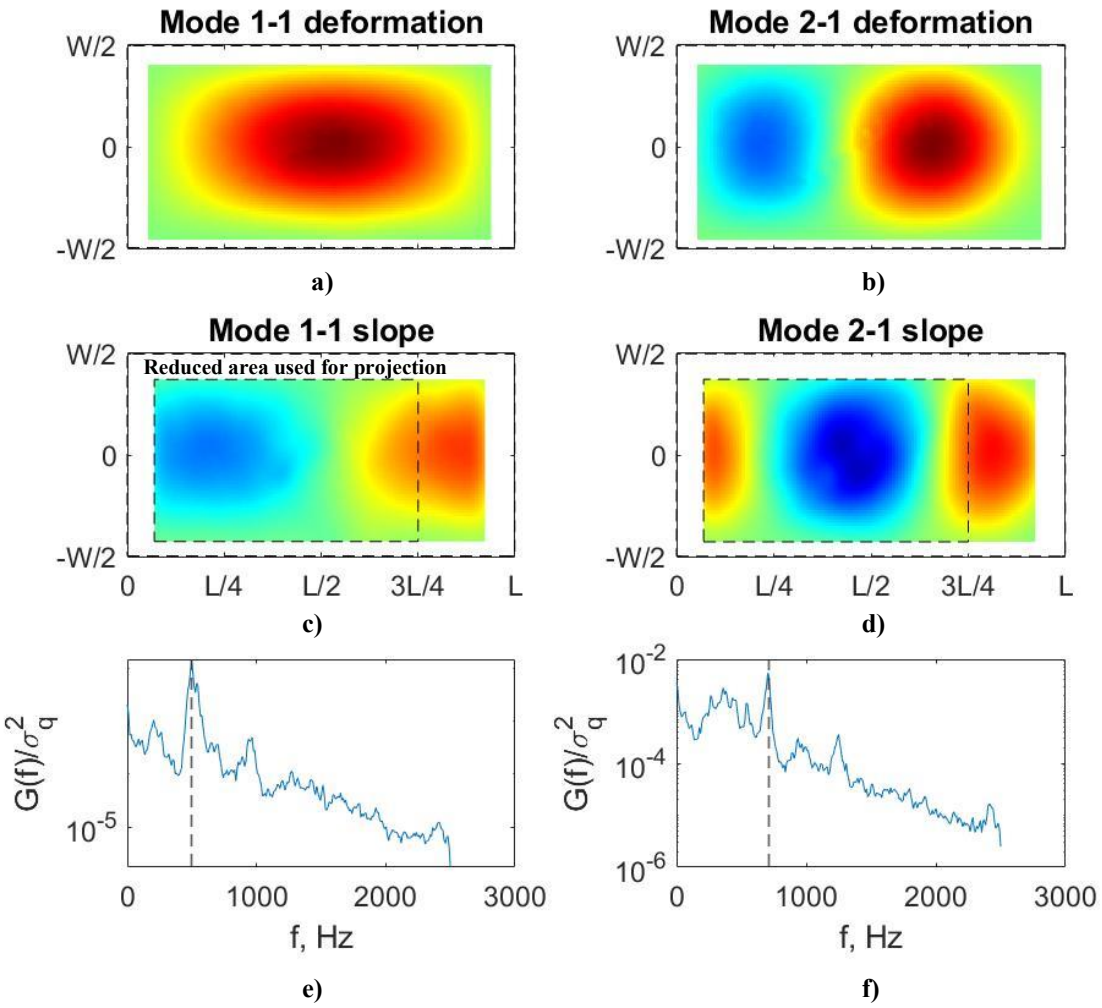

Figure 13: Projection of upstream pressure onto slope of mode shapes; (a-b) first two bending modes, (c-d) streamwise slopes of first two bending modes, (e-f) power spectral density of modal coordinates

V. Reduced order modeling using SINDy algorithm

A different way to capture the coupling between panel vibration and surface pressure is by fitting a differential equation with unknown coefficients to representative time-histories and their derivatives. One algorithm for this task is known as Sparse Identification of Nonlinear Dynamics (SINDy) and was developed by Steve Brunton et al. [17]. The process to obtain an equation of motion from measured data is as follows:

1. First, a set of degrees of freedom is identified, which contain the dominant dynamics of the system. These could be physical degrees of freedom or a reduced set of modal coordinates.
2. A state vector $[\dot{X}]$ is constructed, which contains the temporal derivatives of the DOFs at multiple time instances.
3. Next, the dependent variables are defined that are expected to appear in the equation of motion. A common approach is to use a polynomial library $[\Theta]$, which contains linear and non-linear combinations of the DOFs and their derivatives.
4. A linear system is constructed as such:

$$[\dot{X}] = [\Theta][\xi]$$

   The matrix $[\xi]$ contains the coefficients of the equation of motion, that correspond to terms in the library $[\Theta]$.
5. The linear system is solved for $[\xi]$ using a least squares approach, since it is an overdetermined system.
6. The resulting equation of motion is likely too large and contains contributions from non-linear variables that contribute very little to the overall system dynamics. Thus, the smallest coefficient is discarded and the system is solved again, starting from step #4. At some point, a judgement call needs to be made as to how many coefficients to retain in the differential equation.

An attempt was made to use the SINDY algorithm to find an equation of motion that describes the panel dynamics under the influence of SBLI. In order to set up the differential equation, the highest temporal derivative that plays a dominant role in the system must first be determined. A suitable reference for this case can be found in the literature, where aeroelastic models of compliant panels were created, albeit absent SBLI. Freydin and Dowell [2] derived a reduced order model for a clamped rectangular panel using the Rayleigh-Ritz method. They used a set of linear clamped beam bending mode shapes as basis functions for the panel vibration. After simplification they arrived at the following homogeneous structural equation of motion for the bending modal coordinate w_k:

$$\boldsymbol{M_{nk}\ddot{w}_k + C_{nk}\dot{w}_k + G_{nk}w_k + D_{nkrs}w_k w_r w_s + A_{\dot{w}_{nk}}\dot{w}_k + A_{w_{nk}}w_k - L_{kn}P_k + Q_n = 0}$$

The first three terms are the linear plate model, the next term contains a nonlinear structural stiffness term. The next two terms represent stiffness and damping terms that are a result of aerodynamic coupling. They were derived using piston theory. The seventh term couples the panel deformation to the cavity pressure, which can be important for shallow cavities. The final term Q_n is the static force on the panel that results from static pressure difference between the cavity and freestream pressure. Additional terms such as turbulent pressure forcing or thermoelastic effects are not present in this equation.

Based on this system, a suitable starting point is to assume that the panel dynamics are described by a second order in time system that contains linear stiffness and damping terms. The first three bending modes of the coupled system are used as a basis function and the corresponding modal parameters $w_i = \{w_1, w_2, w_3\}$ are calculated for all time steps. These are now the DOFs used in SINDy. Next, the velocity $\dot{w}_i$ and acceleration $\ddot{w}_i$ are needed. Since these were not measured, they need to be calculated through differentiation of the deformation time histories. Since this is known to amplify noise in the measurement, two steps are implemented to improve this process. First, the data is interpolated, using a cubic spline function, which effectively increases the sampling frequency by a factor of three. Next, the interpolated time histories are differentiated using Tikhonov regularization [21]. This process finds an optimal derivative that penalizes non-smoothness. Note that the original SINDy algorithm uses total variation regularization, which allows for discontinuities in the derivatives. Since the expected derivatives in the plate model are velocities and acceleration, discontinuities are not expected and thus the Tikhonov regularization was utilized, which results in smoother derivatives. The resulting system of equations that is solved is as follows:

$$\begin{bmatrix} \dot{w}_1(t_1) & \dot{w}_2(t_1) & \dot{w}_3(t_1) & \ddot{w}_1(t_1) & \ddot{w}_2(t_1) & \ddot{w}_3(t_1) \\ \vdots & \vdots & \vdots & \vdots & \vdots & \vdots \\ \dot{w}_1(t_N) & \dot{w}_2(t_N) & \dot{w}_3(t_N) & \ddot{w}_1(t_1) & \ddot{w}_2(t_1) & \ddot{w}_3(t_1) \end{bmatrix} =$$

$$[\dot{X}] \in \mathbb{R}^{N\times 6}$$

$$\begin{bmatrix} w_1(t_1) & w_2(t_1) & w_3(t_1) & \dot{w}_1(t_1) & \dot{w}_2(t_1) & \dot{w}_3(t_1) & q_1(t_1) & q_2(t_1) & q_3(t_1) \\ \vdots & \vdots & \vdots & \vdots & \vdots & \vdots & & & \\ w_1(t_N) & & & & & & & & \end{bmatrix}$$

$$[\Theta] \in \mathbb{R}^{N\times 9}$$

$$\times \begin{bmatrix} \xi_{11} & \xi_{12} & \xi_{13} & \xi_{14} & \xi_{15} & \xi_{16} \\ \xi_{21} & \xi_{22} & \xi_{23} & \cdots & & \\ \vdots & \vdots & \vdots & \vdots & \vdots & \vdots \\ \xi_{91} & & & & & \xi_{96} \end{bmatrix}$$

$$[\xi] \in \mathbb{R}^{9\times 6}$$

The matrix $[\dot{X}]$ contains the velocity and acceleration of the modal coordinates at $N = 1000$ time steps. The matrix $[\Theta]$ is of the same size but contains the displacement and velocity as well as forcing terms q_i. The forcing terms are modal projections of the surface pressure field onto the first three mode shapes, thus they use the same basis function as the deformation. The coefficient matrix $[\xi]$ is of size 6×6. As an example, when the system is solved, the coefficient ξ_{16} will tell how much the acceleration $\ddot{w}_3$ depends on the variable w_1.
The system is then solved and rearranged to resemble the equation of motion shown above:

$$\begin{pmatrix} \ddot{w}_1 \\ \ddot{w}_2 \\ \ddot{w}_3 \end{pmatrix} + \underbrace{\begin{bmatrix} -\xi_{44} & -\xi_{54} & -\xi_{64} \\ -\xi_{45} & -\xi_{55} & -\xi_{65} \\ -\xi_{46} & -\xi_{56} & -\xi_{66} \end{bmatrix}}_{\text{Damping matrix}} \begin{pmatrix} \dot{w}_1 \\ \dot{w}_2 \\ \dot{w}_3 \end{pmatrix} + \underbrace{\begin{bmatrix} -\xi_{14} & -\xi_{24} & -\xi_{34} \\ -\xi_{15} & -\xi_{25} & -\xi_{35} \\ -\xi_{16} & -\xi_{26} & -\xi_{36} \end{bmatrix}}_{\text{Stiffness matrix}} \begin{pmatrix} w_1 \\ w_2 \\ w_3 \end{pmatrix} = \underbrace{\begin{bmatrix} \xi_{74} & \xi_{84} & \xi_{94} \\ \xi_{75} & \xi_{85} & \xi_{95} \\ \xi_{76} & \xi_{86} & \xi_{96} \end{bmatrix}}_{\text{Forcing matrix}} \begin{pmatrix} q_1 \\ q_2 \\ q_3 \end{pmatrix}$$

The recovered system contains a single stiffness and a single damping matrix. It is not possible to separate the contributions of the structure and those of the piston-theory aerodynamics or other coupling mechanisms from this approach. This means C_{nk} and $A_{\dot{w}_{nk}}$ are combined, as well as G_{nk} and $A_{w_{nk}}$. The recovered stiffness matrix is mostly diagonal, with off-diagonal terms being an order of magnitude smaller. An ideal linear structural system would have purely diagonal terms, which represent the squares of the natural frequencies. An analysis is performed, in which the obtained natural frequencies for the three modes are computed and compared to the true natural frequencies of the system, which are the dominant frequencies in the measured deformation spectra. The total length of the recording was split up into 6 segments of equal length and the system identification was performed for each of these segments separately. The resulting stiffness, damping, and forcing matrices were compared to evaluate consistency of the results. A properly identified differential equation should be valid for the entire time-history and only slight changes due to noise and errors introduced from numerical differentiation are expected. Results show that the identified coefficients for the stiffness matrix are consistent, e.g., the standard deviation of their values is an order of magnitude less than the coefficients.
The frequencies identified from the diagonal entries of the stiffness matrix are plotted in Figure 14 for each of the six segments. They show little variance and agree well with the true natural frequencies. The results are sensitive to the choice of regularization parameters. Reasonable values were obtained by adjusting the regularization parameters such that the identified natural frequencies from SINDy match with the true values. It was further observed that the consistency of the identified frequencies was not much affected by the regularization parameters, meaning the variance

of coefficients identified from different time segments remained mostly the same. The diagonal terms of the linear stiffness matrix were the only consistent results that were obtained from the SINDy algorithm. Neither the forcing nor damping matrix showed consistency. It remains to be seen, whether this is due to measurement noise or an incorrect choice of basis functions.

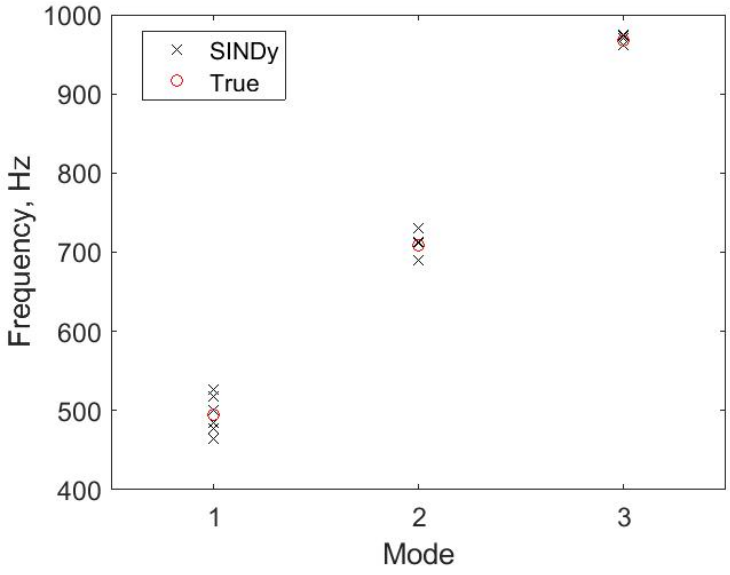

Figure 14: Identified natural frequencies from SINDy algorithm

VI. Conclusion

This paper investigated several low order modeling techniques to analyze the dynamics of a compliant panel under a ramp induced SBLI. A single DOF reconstruction of the surface pressure field was created by fitting linear functions to the SBLI-induced pressure rise and thus extracting the shock foot motion. Comparison between the pressure field on the rigid and compliant panel showed no difference in the streamwise extent of the shock foot motion. It was however shown that the shock motion locks into the first resonant frequency of the panel bending vibration, thus showing clear evidence of fluid-structure interaction.

Comparison of the POD modes of the surface pressure on the rigid and compliant panel showed that the lower modes are very similar, neither the mode shapes nor the power spectra of their time-histories change significantly. The first POD mode oscillates slightly at the first bending frequency, though the spectrum is still dominated by low-frequency broadband motion. The sixth POD mode of the compliant panel shows a very dominant peak at the first resonant frequency. The mode shape clearly shows the streamwise motion of the shock foot. These results show that while the shock motion is clearly influenced by the panel vibration, this is a secondary effect. The dominant surface pressure fluctuations (the first five POD modes) seem to be little affected by the panel compliance in this case.

A clear relation between the surface pressure field upstream of the shock and the slope of the panel deformation was shown, using a projection method. This result confirms previous findings that demonstrate that first order piston theory can adequately describe the fluid dynamics in that region and that PSP can accurately capture these subtle relations.

The SINDy algorithm was used to find an equation of motion for the panel dynamics. The first three mode shapes were used as basis functions and the deformation and pressure were projected onto them, to obtain three degrees of freedom respectively for pressure (forcing) and bending deformation (response). A reasonable stiffness matrix was identified, that was dominated by diagonal terms and resulted in expected resonant frequencies. The results were consistent and errors are likely a result of measurement noise. Unfortunately, no other consistent coefficients in the equation of motion could be identified. It is unclear if this is due to measurement noise or because a wrong form of

the assumed equation of motion was used. A variety of basis functions and terms was chosen but, in all cases, only the linear stiffness matrix was consistently recovered. Investigations are currently underway in which a more detailed numerical model of the aeroelastic plate vibration is implemented (without SBLI) and the results are then input into the SINDy algorithm. This allows identification of sensitivity to noise and thus the feasibility of obtaining an equation of motion for the more involved system with SBLI can be better evaluated.

Appendix

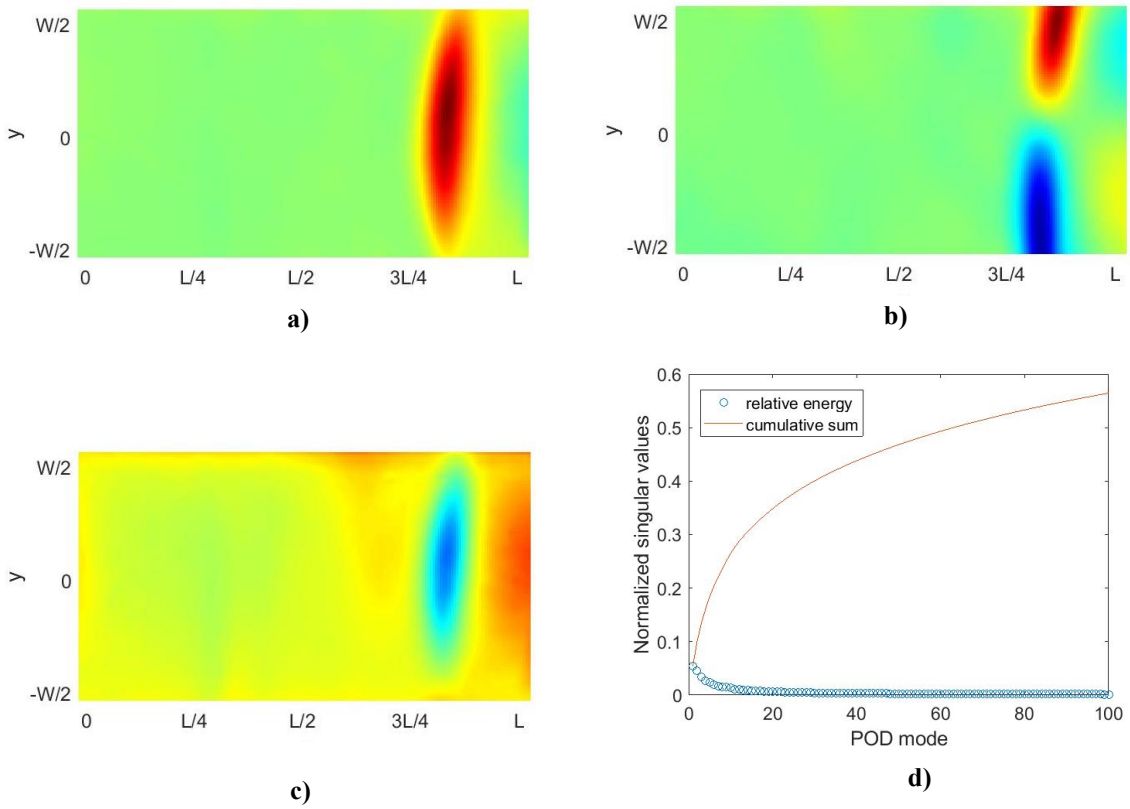

Figure 15: POD of compliant panel surface pressure; (a) first mode, (b) second mode, (c) third mode and (d) singular values

Acknowledgments

This work was supported by the National Science Foundation under award #1913587. The authors would like to thank Dr. Jeremy Jagodzinski for assisting with the measurements.

References

[1] J. J. McNamara and P. P. Friedmann, "Aeroelastic and Aerothermoelastic Analysis in Hypersonic Flow: Past, Present, and Future," *AIAA journal,* vol. 49, no. 6, pp. 1089-1122, 2011.

[2] M. Freydin and E. Dowell, "Nonlinear Theoretical Aeroelastic Model of a Plate: Free to Fixed In-plane Boundaries," *AIAA journal,* vol. 59, no. 2, pp. 447-461, 2021.

[3] T. J. Whalen, S. J. Laurence, B. Sullivan, D. J. Bodony and M. Freydin, "Hypersonic Fluid–Structure Interactions in Compression Corner Shock-Wave Boundary-Layer Interaction," *AIAA journal,* vol. 59, no. 8, pp. 4090-4105, 2019.

[4] M. S. Spottswood, T. J. Beberniss, T. G. Eason, R. A. Perez, J. M. Donbar, D. A. Ehrhardt and Z. B. Riley, "Exploring the response of a thin, flexible panel to shock-turbulent boundary-layer interactions," *Journal of Sound and Vibration,* vol. 443, pp. 74-89, 2019.

[5] K. R. Brouwer, R. A. Perez, T. J. Beberniss, S. M. Spottswood, D. A. Erhardt and R. Wiebe, "Investigation of aeroelastic instabilities for a thin panel in turbulent flow," *Nonlinear Dynamics,* vol. 104, no. 4, pp. 3323-3346, 2021.

[6] M. R. Visbal, "Viscous and inviscid interactions of an oblique shock with a flexible panel," *Journal of Fluids and Structures,* vol. 48, pp. 27-45, 2014.

[7] J. D. Thayer, J. J. McNamara and D. V. Gaitonde, "Unsteady Aerodynamic Response of a High-Speed, Separated Flow to a Deforming Cantilever Plate," in *AIAA paper 2022-0292, Scitech 2022 Forum*, San Diego, CA, 2022.

[8] M. Eitner, Y. Ahn, M. Musta, L. Vanstone, J. Sirohi and N. Clemens, "Effect of Shock Wave Boundary Layer Interaction on Vibratory Response of a Compliant Panel," in *AIAA Aviation Forum*, 2021.

[9] M. C. Neet and J. M. Austin, "Effects of Surface Compliance on Shock Boundary Layer Interaction in the Caltech Mach 4Ludwieg Tube," in *AIAA Scitech Forum*, 2020.

[10] S. Tan, P. Bruce and M. Gramola, "Oblique Shockwave Boundary Layer Interaction on a Flexible Surface," in *AIAA Scitech Forum*, 2019.

[11] A. Tripathi, J. Gustavsson, K. Shoele and R. Kumar, "Response of a Compliant Panel to Shock Boundary Layer," in *AIAA Scitech Forum*, 2021.

[12] M. N. Musta, L. Vanstone, Y.-J. Ahn, M. Eitner, Jayant Sirohi and N. Clemens, "Investigation of flow-structure coupling for a compliant panel under a shock/boundary-layer interaction using fast-response PSP," in *AIAA AVIATION 2021 FORUM*, Virtual, 2022.

[13] S. Varigonda and V. Narayanaswamy, "Investigation of Shock Wave Oscillations over a Flexible Panel in Supersonic Flows," in *AIAA Aviation Forum*, 2019.

[14] P. B. Vasconcelos, L. P. McQuellin, T. Krishna and A. Neely, "Experimental Study of Hypersonic Fluid-Structure Interactions on an Inclined Clamped-Free-Clamped-Free Compliant Panel," in *AiAA paper 2021-4232, ASCEND 2021*, 2021.

[15] Y.-J. Ahn, M. N. Musta, M. A. Eitner, J. Sirohi and N. T. Clemens, "Experimental Investigation of Flow-Structure Interaction for a Compliant Panel under a Mach 2 Compression-Ramp," in *AIAA paper 2022-0293, Scitech Forum*, San Diego, CA, 2022.

[16] S. Willems, A. Gülhan and B. Esser, "Shock induced fluid-structure interation on a flexible wall in supersonic turbulent flows," in *EUCASS Proceedings Series - Advances in Aerospace Sciences*, 2013.

[17] S. L. Brunton, J. L. Proctor and J. N. Kutz, "Discovering governing equations from data by sparse identification of nonlinear dynamical systems," *Proceedings of the National Academy of Sciences,* vol. 113, no. 15, pp. 3932--3937, 2016.

[18] D. Gorjup, "Laboratory for Dynamics of Machines and Structures at the University of Ljubljana, Slovenia - speckle_pattern.py," 2018. [Online]. Available: https://github.com/ladisk/speckle_pattern/blob/master/LICENSE.

[19] M. E. Erengil and D. S. Dolling, "Unsteady Wave Structure near Separation in a Mach 5 Compression Ramp Interaction," *AIAA journal,* vol. 29, no. 5, pp. 728-735, 1991.

[20] E. H. Dowell, Aeroelasticity of Plates and Shells, Springer, 1974.

[21] J. Wagner, "Jakub Wagner (2022). Regularised numerical differentiation (https://www.mathworks.com/mMatlab File Exchange - Regularised-numerical-differentiation," 2022. [Online]. Available: https://www.mathworks.com/matlabcentral/fileexchange/74165-regularised-numerical-differentiation.